



Explaining JWST Counts with Galaxy Formation Models

Giorgio Manzonì¹, Tom Broadhurst^{2,3,4}, Jeremy Lim⁵, Tao Liu^{6,1}, George Smoot^{1,6,7,8,9,10,19}, Carlton M. Baugh¹¹, Scott Tompkins¹², Rogier Windhorst¹³, Simon Driver¹², Timothy Carleton¹³, Brenda Frye¹⁴, Leo Fung^{15,11}, Jiashuo Zhang⁵, Seth H. Cohen¹³, Christopher J. Conselice¹⁶, Norman A. Grogin¹⁷, Rolf A. Jansen¹³, Anton M. Koekemoer¹⁷, Rafael Ortiz, III¹³, Norbert Pirzkal¹⁷, and Christopher N. A. Willmer¹⁸

¹ Jockey Club Institute for Advanced Study, The Hong Kong University of Science and Technology, Hong Kong S.A.R., People's Republic of China

² Department of Theoretical Physics, University of the Basque Country UPV-EHU, E-48040 Bilbao, Spain

³ Donostia International Physics Center (DIPC), 20018 Donostia, The Basque Country, Spain

⁴ IKERBASQUE, Basque Foundation for Science, Alameda Urquijo, 36-5 E-48008 Bilbao, Spain

⁵ Department of Physics, The University of Hong Kong, Pokfulam Road, Hong Kong

⁶ Department of Physics, The Hong Kong University of Science and Technology, Clear Water Bay, Kowloon, Hong Kong S.A.R., People's Republic of China

⁷ DIPC, Basque Country UPV/EHU, E-48080 San Sebastian, Spain

⁸ Energetic Cosmos Laboratory, Nazarbayev University, Nursultan, Kazakhstan

⁹ Physics Department, University of California at Berkeley, Berkeley, CA 94720, USA

¹⁰ Paris Centre for Cosmological Physics, APC, AstroParticule et Cosmologie, Université de Paris, CNRS/IN2P3, CEA/Irfu, Université Sorbonne Paris Cité, 10, rue Alice Domon et Leonie Duquet, 75205 Paris CEDEX 13, France

¹¹ Institute for Computational Cosmology (ICC), Department of Physics, Durham University, South Road, Durham, DH1 3LE, UK

¹² International Centre for Radio Astronomy Research (ICRAR) and the International Space Centre (ISC), The University of Western Australia, M468, 35 Stirling Highway, Crawley, WA 6009, Australia

¹³ School of Earth and Space Exploration, Arizona State University, Tempe, AZ 85287-1404, USA

¹⁴ Department of Astronomy/Steward Observatory, University of Arizona, 933 N Cherry Ave, Tucson, AZ 85721-0009, USA

¹⁵ Centre for Extragalactic Astronomy, Department of Physics, Durham University, South Road, Durham, DH1 3LE, UK

¹⁶ Jodrell Bank Centre for Astrophysics, Alan Turing Building, University of Manchester, Oxford Road, Manchester, M13 9PL, UK

¹⁷ Space Telescope Science Institute, 3700 San Martin Drive, Baltimore, MD 21218, USA

¹⁸ Steward Observatory, University of Arizona, 933 N Cherry Ave, Tucson, AZ 85721-0009, USA

Received 2025 February 18; revised 2025 June 3; accepted 2025 June 3; published 2025 July 29

Abstract

A distinct power-law break is apparent at $m_{AB} \sim 21$ in the deep near-infrared PEARLS-JWST galaxy counts. The break becomes more pronounced at longer wavelengths, with the slope flattening smoothly with apparent magnitude in the shortest band used at $0.9 \mu\text{m}$, and trending toward an increasingly broken slope by the longest wavelength passband of JWST's Near Infrared Camera, $4.4 \mu\text{m}$. This behaviour is remarkably well predicted by the GALFORM semi-analytical model of galaxy formation. We use the model to diagnose the origin of this behaviour. The features that are responsible for the break are (1) the inherent break in the luminosity function (LF); (2) the change in the volume element with redshift; (3) the redshift-dependent nature of the k -correction (with 1 contributing to the existence of the break and 2–3 contributing to its shape). We study the contribution to these effects by their morphology using the bulge-to-total stellar mass ratio. The way in which bulge-dominated galaxies populate the bright end of the LF while disk-dominated galaxies dominate the faint end is preserved in the galaxy number counts, with a characteristic stellar mass at a break of $\sim 10^{10} M_{\odot}$. The shape of the number counts is mainly driven by galaxies with relatively low redshift ($z \lesssim 2$) for a limit of $m_{AB} \lesssim 28$. We give a comprehensive description of why the galaxy number counts in the near-infrared PEARLS-JWST observation look the way they do and which population of galaxies is dominant at each apparent magnitude.

Unified Astronomy Thesaurus concepts: Galaxy formation (595); Galaxy counts (588); Galaxy evolution (594); Observational cosmology (1146); James Webb Space Telescope (2291); Astronomical simulations (1857); Hierarchical models (1925); Cosmological models (337)

Materials only available in the online version of record: figure set

1. Introduction

Study of galaxy number counts, tracing objects from ultraviolet to submillimeter wavelengths, has evolved from a tool for mapping local structure (W. Herschel 1785; J. C. Kapteyn 1922; F. H. Seares et al. 1925; H. Shapley & A. Ames 1932; E. Hubble 1934; F. Zwicky 1937) to a critical

test of galaxy evolution models in the era of multiwavelength surveys (A. Sandage 1961; T. W. Noonan 1971; B. M. Tinsley 1977, 1980; T. Shanks et al. 1984; L. R. Jones et al. 1991; N. Metcalfe et al. 1991; T. J. Broadhurst et al. 1992; L. L. Cowie et al. 1994; S. P. Driver et al. 1995; K. Glazebrook et al. 1995; L. L. Cowie et al. 1996; J. P. Gardner et al. 1996; N. Yasuda et al. 2001; A. Cooray 2016; J. H. Marr 2023).

The study of the number counts at different wavelengths is crucial as galaxies have completely different behaviors moving from the submillimeter, infrared, optical, to ultraviolet. S. P. Driver et al. (1994) made one of the first multiwavelength analyses of number counts, using four different optical filter measurements with the aim of constraining a model in which dwarf galaxies play a special role in addressing the faint blue

¹⁹ Emeritus.



galaxy excess. All multiwavelength studies of number counts rely on precise modeling of the k -correction to convert the flux received in the observer frame to the flux emitted in the rest frame of the galaxy (G. D. Coleman et al. 1980; D. W. Hogg 1999; M. R. Blanton & S. Roweis 2007). This k -correction can be very different for different galaxy types as it relies on the associated shape of the spectral energy distribution (SED). One advantage of near-infrared wavelengths is that the SEDs of different galaxy types remain roughly self-similar (see, e.g., Figure 1 of L. L. Cowie et al. 1994). Thanks to the ability of the Wide Field Camera 3 on the Hubble Space Telescope (HST) to attain high-resolution imaging and spectroscopy from the ultraviolet to the near-infrared, R. A. Windhorst et al. (2011) revitalized interest in galaxy counts, showing their relation to the extragalactic background light (EBL). Since the EBL can be used to construct cosmic-ray attenuation models, R. A. Windhorst et al. (2011) highlighted the importance of galaxy number counts also in practical applications. The relation between number counts and EBL was initially analyzed by P. Madau & L. Pozzetti (2000), where they showed that for the EBL to converge, the slope of the count has to be smaller than 0.4, which is what happens in every band at fainter magnitudes, while for the brighter part it is approximately 0.6. This implies that a broken power law in the counts is needed to have a finite EBL, and the galaxies dominating the break are those contributing the most to the EBL. Intuitively, a flattening of the slope of the galaxy number counts can be seen as a balance between an increasing number of faint galaxies and a decreasing of the individual flux contribution due to cosmological dimming. This flattening was already observed both in the optical and in the infrared by early studies from J. P. Gardner et al. (1993) and I. Smail et al. (1995). S. P. Driver et al. (2016) further scrutinized the relation between galaxy number counts and EBL, showing additional effects related to different galaxy populations and galaxy evolution processes. This suggests that to attain a comprehensive view of the processing regulating the shape of the number counts and their relation to the EBL, galaxy formation models are an excellent resource.

More recent multiwavelength studies have further scrutinized the behavior of infrared and submillimeter galaxy counts, confirming the double power-law behavior (e.g., D. L. Shupe et al. 2008; B. Altieri et al. 2010; M. Béthermin et al. 2012; M. L. N. Ashby et al. 2013; J. A. Zavala et al. 2017; S. M. Stach et al. 2018). In addition, other studies have tried to model the galaxy properties to obtain better fits to the data (e.g., C. Gruppioni et al. 2011; S. J. Kim et al. 2024; M. Rowan-Robinson 2024), usually attributing great importance to dust obscuration, the presence of active galactic nuclei (AGNs) activity, or the parameterization of the star formation history. Some key open questions still await a definitive answer. Are galaxy evolution processes enough to describe the extent of the break in the galaxy counts? Are these processes as important as cosmological effects, or can they be treated as a second-order correction? Can new populations of high-redshift galaxies alter the behavior of the faint end of the counts? Can infrared galaxy number counts give us constraints on the nature of dark matter?

To answer these questions, we decided to use the GALFORM semi-analytical model of galaxy formation (S. Cole et al. 2000; C. G. Lacey et al. 2016) and test it on JWST near-infrared number counts collected by the PEARLS team (R. A. Windhorst et al.

2023). The wide filters of the Near Infrared Camera (NIRCam) on JWST can cover the reddest part of the optical spectrum at $0.7\ \mu\text{m}$ up to the near-infrared part at $4.4\ \mu\text{m}$, while the Mid-Infrared Instrument covers $4.9\text{--}28.8\ \mu\text{m}$. The PEARLS team collected exquisite NIRCam images of two unbiased fields that they used to provide accurate deep number counts in the $0.9\text{--}4.4\ \mu\text{m}$ window (R. A. Windhorst et al. 2023). Combining these new observations for the faint part of the number counts with results from previous brighter surveys such as GAMA (S. P. Driver et al. 2011) and DEVILS (L. J. M. Davies et al. 2021), the “knee” at about $m_{\text{AB}} \sim 20$ is clearly visible, offering a perfect observational sample for our analysis. This behavior has been previously predicted by galaxy formation models (see, e.g., W. I. Cowley et al. 2018; L. Y. A. Yung et al. 2022). In this work, after checking that the model predictions accurately reproduce the observations, we take advantage of the additional information coming from the model to deconstruct the galaxy number counts into constituent luminosity functions (LFs), and put together a comprehensive explanation of how the break in the counts originates and the role that different galaxy populations have at different redshifts.

The motivation of this study is to provide a solid and physically motivated framework of what we can and cannot infer from the shape of the number counts. This work is timely because with JWST there is a renewed interest in faint high-redshift objects. This could lead to the misconception that the faint part of the number counts is extremely sensitive to the presence or absence of these extremely high-redshift faint objects. Although we do not completely exclude the possibility that high-redshift objects can slightly affect the very faint end of the number counts, in this study we show that up to the sensitivity of the PEARLS observation ($m_{\text{AB}} \lesssim 28$) we can accurately reproduce the shape of the counts by using only LFs below a redshift of 2. In fact, we compared the results of the counts constructed with LFs with $z < 2$, finding a difference to the total counts of only 0.14 ± 0.03 dex in the faint end. This suggests that the faint end of the galaxy number counts on its own is not sufficient to infer the nature of dark matter, because it is still dominated by the luminosity of these low-redshift objects. By giving a fully comprehensive explanation of the factors that shape the number counts, we hope to set the ground for further studies that aim to interpret the physics behind galaxy statistics, in particular by identifying all the observational biases that arise from the change in reference frame in an expanding Universe.

In Section 2, we outline the GALFORM semi-analytical model and the PEARLS observations that we will compare our predictions to; in Section 3, we present our results, starting from our prediction for the galaxy number counts to their interpretation in terms of galaxy populations and the role they play in the origin of the break; finally, in Section 4, we summarize our findings and conclusions.

In this study, we adopt the cosmology from Planck Collaboration et al. (2014) consisting of $H_0 = 67.3$, $\Omega_{\Lambda} = 0.685$, $\Omega_m = 0.315$, and $\sigma_8 = 0.829$.

2. Methodology

2.1. The GALFORM Model

To make predictions for observable quantities using a physical model, we use the GALFORM semi-analytical galaxy formation model (S. Cole et al. 2000).²⁰ GALFORM follows the

²⁰ The version of GALFORM used here is version 2.7.0 as built by the corresponding author on 2022 December 7, 09:25:24 GMT.

hierarchical formation and growth of dark matter halos, the sites of galaxy formation, as well as modeling the main processes regulating the baryonic component and the formation of galaxies. Here, the dark matter halo merger histories are based on the extended Press–Schechter theory combined with a Monte Carlo approach (C. Lacey & S. Cole 1993). This technique allows us to predict the probability of having a progenitor/descendant halo of a specific mass at a specific redshift, as is needed to generate merger histories (S. Cole et al. 2000). This in turn lets us target halos that are expected to contribute to the number counts. An alternative technique to create a merger history of dark matter halos is to use N -body simulations (e.g., G. Manzoni et al. 2024). H. Parkinson et al. (2008) showed that results based on N -body simulations are in agreement with the extended Press–Schechter theory.

The main galaxy formation processes modeled by GALFORM are extensively discussed in C. G. Lacey et al. (2016). Important processes include the effect of dark matter on baryons, the creation of galactic disks through shock heating, radiative gas cooling, quiescent star formation, starbursts driven by merger instabilities, feedback driven by supernovae, AGNs and photoionization, and dust attenuation.

These processes are modeled through a set of coupled differential equations with a set of parameters as listed in Table 1 of C. G. Lacey et al. (2016). Here, we chose the values for those parameters as in C. M. Baugh et al. (2019). The way these values are chosen is described in C. G. Lacey et al. (2016) and C. M. Baugh et al. (2019). Those authors used a set of observables in the local Universe, and let the parameters vary within a range allowed by theory. Once the parameters are set, the predictive power of GALFORM is stored in the coupled differential equations. Alternative approaches to determine the best values for the parameters are described in E. J. Elliott et al. (2021) and M. Madar et al. (2024). To reproduce the results of this work, the parameters in C. M. Baugh et al. (2019) need to be used. The predictions we get from the model for the number counts and all the other observables are the results of this parameter choice, and we stress that we do not change any parameter to reproduce the JWST observations. The remarkable agreement with the observations that we show in this work is the result of the choice of parameters in C. M. Baugh et al. (2019) and GALFORM differential equations.

2.2. The PEARLS Observations

The Prime Extragalactic Areas for Reionization and Lensing Science (PEARLS) is a scientific project led by R. Windhorst that takes advantage of the 110 hr of guaranteed time on JWST to study the very early Universe, and in particular the assembly of galaxies, with unprecedented precision (R. A. Windhorst et al. 2023). Among the different PEARLS targets, two of them are suitable for number counts because of the absence of foreground objects. These are the JWST IRAC Dark Field (JWIDF) and the El Gordo noncluster module.²¹ The JWIDF and the El Gordo noncluster module cover $61''.2 \times 109''.3$ and $134''.0 \times 132''.7$, respectively (see Figures 2 and 3 of R. A. Windhorst et al. 2023). For these targets, they performed photometry in seven NIRCам wide filters covering the 0.9–4.4 μm window, with a depth of $m_{\text{AB}} \lesssim 28$.

To create the catalog used for the number counts, they ran SourceExtractor (E. Bertin & S. Arnouts 1996) and ProFound (A. S. G. Robotham et al. 2018) on the NIRCам reduced images. The star–galaxy separation procedure that has been used to clean stars from the catalog in both fields is based on the FWHM versus apparent magnitude plot. The algorithm is described in R. A. Windhorst et al. (2011). To complement the deep and faint NIRCам counts, R. A. Windhorst et al. (2023) collected data from brighter surveys, including GAMA (S. P. Driver et al. 2011) and DEVILS (L. J. M. Davies et al. 2021); for the shorter-wavelengths filters, they also used the deepest HST counts available. For a complete description of the complementary data used here, see S. Koushan et al. (2021). Here, all the data used for the number counts are shown in Figure 1 as gray dots and their relative fit as a blue line (compare the original data from Figures 9 and 10 in R. A. Windhorst et al. 2023). Note that the fit extends brightward and faintward of the magnitude range actually sampled by the data.

3. Results

3.1. Testing the Model Prediction

We now test the model against the observations collected by the PEARLS team in R. A. Windhorst et al. (2023). In their Figures 9 and 10, they show fits to the galaxy number counts for the JWST/NIRCам filters in the range 0.9–4.4 μm and other brighter surveys both from space and the ground. We plot the observations from R. A. Windhorst et al. (2023) with gray dots and their fits with a blue line in Figure 1, where we compare them to the simulated galaxy counts in two representative filters (orange lines). F090W (left panel) is the shortest-wavelength filter used by the PEARLS team, centered at $\sim 0.90 \mu\text{m}$, while F444W (right panel) is the longest-wavelength filter, centered at $\sim 4.44 \mu\text{m}$.

We performed a separate power-law fit to the simulated counts for the bright (apparent magnitude between 10 and 20, black solid line) and faint (apparent magnitude between 25 and 30, black dashed line) parts of the counts, which tend to power laws. We will refer to the intersection between the two linear fits as the knee of the counts. We performed a linear fit in the log-plane using ordinary least-squares regression and estimating the uncertainties on the parameters as standard errors. We report the parameters of the fits in the legend of Figure 1. It is interesting to note that the slope of the power law in the faint regime is very similar at both wavelengths, with 0.190 ± 0.002 for the F090 filter and 0.195 ± 0.001 for the F444W filter. A bigger difference between the two filters is seen, however, at brighter apparent magnitudes, with a slope of 0.551 ± 0.004 found for the F090W counts compared with 0.656 ± 0.007 for the F444W counts, making the knee more pronounced at longer wavelengths. We will give a full explanation of this feature in Sections 3.2 and 3.6, and report the slope for each band in Table 1. We anticipate that this effect is due to a combination of band shifting and cosmological dimming due to the increasing redshift when this combines with the shape of the SED of the objects considered. Our model can reproduce the observed counts quite accurately, with a small offset in the faint end of the counts in F444W. Most importantly, it is impressively accurate in predicting the slope of the double power law in all the filters, implying that the physics responsible for the knee is included in the GALFORM

²¹ Named as such as it is slightly offset by the El Gordo cluster.

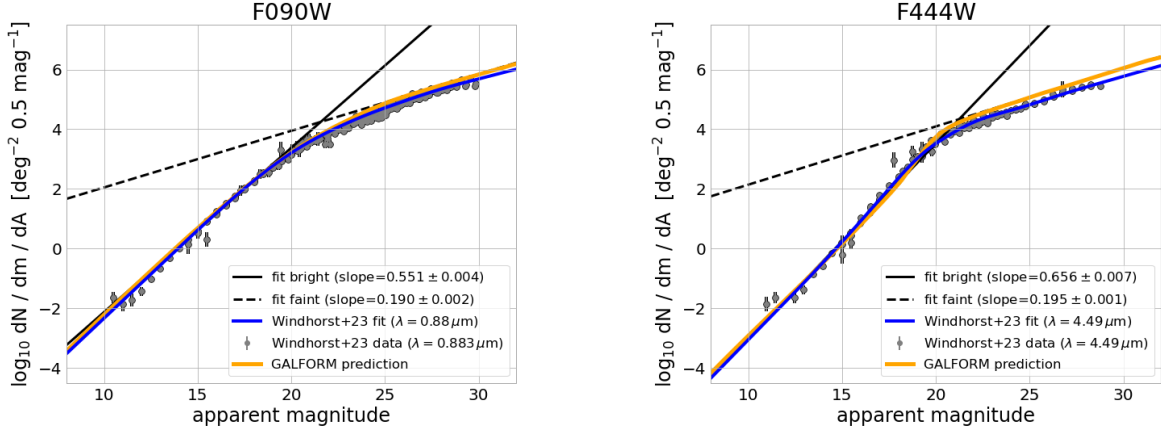


Figure 1. Number counts predicted using GALFORM (orange lines) together with the data collected in R. A. Windhorst et al. (2023, gray dots) and the respective double power-law fits (blue lines). In the left panel, we plot the counts for the shortest-wavelength filter used by R. A. Windhorst et al. (2023), which is the NIRCcam F090W, while in the right panel, we show the longest-wavelength counts, which is the F444W. The break in the counts’ slope is more pronounced at longer wavelengths. The black lines are power-law fits to the GALFORM counts when considering separately the results on the left and right sides of the break. The intersection of these two lines can be used to precisely locate the break or change in the slope of the counts.

(The complete figure set (8 images) is available in the [online article](#).)

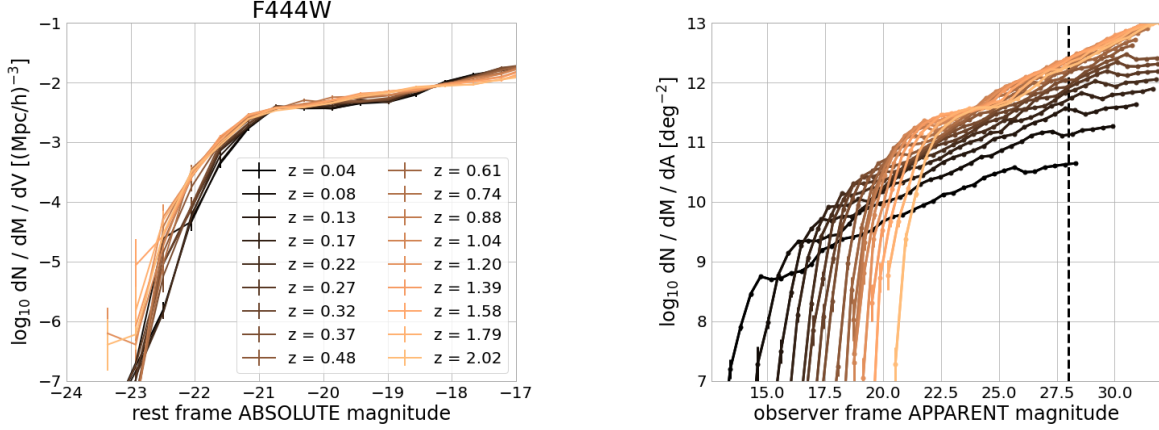


Figure 2. Luminosity functions (LFs) predicted by GALFORM at closely spaced redshifts in the range $0 < z < 2$, as shown by the key, for the long-wavelength F444W filter. Left: we plot the LFs and their Poisson errors in the traditional rest-frame absolute magnitudes vs. number of objects per unit magnitude and unit volume. Right: we plot the LFs in units of number counts, i.e., observer-frame apparent magnitudes vs. number of objects per unit magnitude and unit area. Error bars indicate their Poisson error. The number counts are derived from the integration of the LFs in these units over the redshift range covered by the apparent magnitude limit (for PEARLS observations, this limit is approximately at F444W ~ 28). It can be seen how the effect of cosmological dimming and k -correction moves the LFs horizontally, while the change in volume for a fixed area moves the LFs vertically. The combination of these effects leads to the break we see in the counts. To compare this effect in all of the NIRCcam wide filters, see the components of the associated Figure Set.

Observer-frame luminosity functions for all the NIRCcam filters (analog to the right panel of Figure 2).

(The complete figure set (8 images) is available in the [online article](#).)

modeling. This also excludes the possibility of blaming new physics for this clear feature in the galaxy number counts. Although we chose to include only the counts for these two representative filters, we note that the GALFORM model can reproduce with the same level of agreement the counts observed in the other JWST/NIRCcam filters used in PEARLS, and we report them in Figure Set 1, available in the online version. The GALFORM counts from W. I. Cowley et al. (2018) have been reported to enjoy varying levels of agreement with observations made in other bands observed with JWST (e.g., C.-T. Ling et al. 2022; C. K. W. Wu et al. 2023; G. Yang et al. 2023; L. Sajkov et al. 2024; M. A. Stone et al. 2024). We emphasize that both in this work and in W. I. Cowley et al. (2018) the choice of the parameters controlling GALFORM

come from previous calibrations on local LFs and have not been altered to fit the JWST observations (see also S. Lu et al. 2025). Here, we use the parameters derived from the calibration in C. M. Baugh et al. (2019).

3.2. Interpretation of the Break in the Counts

One of the key advantages of using a galaxy formation model to interpret the shape of the number counts is that we can deconstruct the counts into the sum of different LFs at specific redshifts corresponding to the outputs of the simulations. This would be extremely complicated to do with observational data only. The first reason is that we would need precise spectroscopic redshift measurements; this would defeat the purpose of the number counts as a simple and

Table 1

Slopes for the Bright and Faint Power Laws of the GALFORM Prediction for the Number Counts, as Defined at the Beginning of Section 3.1, for All the NIRCcam Wide Filters

Filter	Slope Bright	Slope Faint
F070W	0.556 ± 0.005	0.192 ± 0.003
F090W	0.551 ± 0.004	0.190 ± 0.002
F115W	0.554 ± 0.005	0.189 ± 0.002
F150W	0.560 ± 0.005	0.190 ± 0.001
F200W	0.575 ± 0.005	0.190 ± 0.001
F277W	0.640 ± 0.005	0.191 ± 0.001
F356W	0.649 ± 0.007	0.194 ± 0.001
F444W	0.656 ± 0.007	0.195 ± 0.001

immediate test. Second, different redshift samples would be affected by different degrees of incompleteness. Moreover, instead of precise redshift outputs, we would need to deal with narrow redshift bins, which would affect the purity of the sample. Another advantage is that in simulations we can select galaxies with different properties to see how they contribute to the number counts.

In Figure 2, we can see the number counts broken down into their constituent LFs. Error bars, indicating the Poisson error on the counts, show the intrinsic scarcity of bright objects compared to the abundance of faint objects. We have tested that we are able to accurately reproduce the shape of the observed number counts by using only LFs with $z \lesssim 2$, even though the maximum output redshift from our calculations is much higher. This is also shown by Figure 3, where we plot the mean redshift as a function of apparent magnitude for the number counts in three representative filters. Up to the PEARLS apparent magnitude limit of $m_{AB} \sim 28$ (indicated by a vertical dashed line) the mean redshift is below $z \lesssim 2$ for all the filters, showing that the shape of the number counts is mainly driven by low-redshift objects. This does not mean that there are no objects at higher redshift, but that considering LFs at higher z would not alter the shape of the total number counts. In fact, we find a negligible difference in the faint end of 0.14 ± 0.03 dex.

The left panel of Figure 2 shows the traditional way of plotting LFs at different redshifts, i.e., using rest-frame absolute magnitudes for the x -axis and the number of objects per unit magnitude and unit volume for the y -axis. Using rest-frame absolute magnitudes means that we are looking at the intrinsic luminosity of the galaxy at the emitted wavelength, ignoring the band shifting and cosmological dimming due to redshift. This way, we can look at the intrinsic properties of the galaxies without worrying about how the redshift affects observations. In this traditional way of plotting LFs, we can see the intrinsic galaxy evolution; for example, we see that at the bright end galaxies were a bit brighter at $z \sim 2$ than at $z \sim 0$, in agreement with the drop in star formation rate density after Cosmic Noon (P. Madau & M. Dickinson 2014). Rest-frame LFs in the infrared, however, vary less than in the optical and ultraviolet, and to show this we performed a fit with Schechter functions to all the LFs plotted in Figure 2. We report the average parameters for ϕ_* , M_* , and α ,²² with

²² For a Schechter function of shape $\Phi(M) = 0.4 \ln(10) \phi_* 10^{0.4(\alpha+1)(M^*-M)} e^{-10^{0.4(M^*-M)}}$, with $\Phi(M)$ being the number density of galaxies per unit magnitude and volume, ϕ_* the characteristic number density ($\text{Mpc}^{-3} \text{mag}^{-1}$), M^* the characteristic absolute magnitude, and α the faint-end slope parameter.

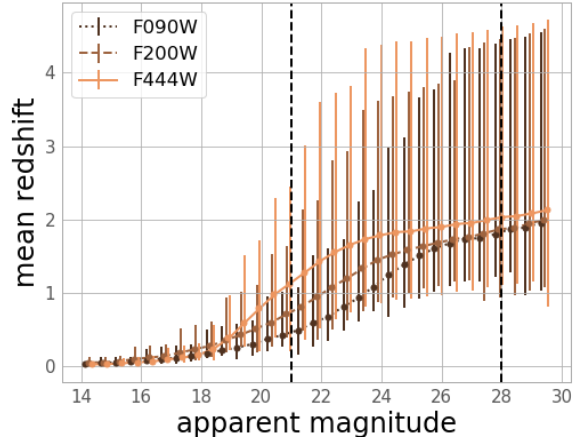


Figure 3. Mean redshift as a function of apparent magnitude for objects simulated in three representative NIRCcam filters: F090W (dark dotted brown line), F200W (brown dashed line), and F444W (light brown solid line). Error bars are the 25th and 75th percentiles of the associated redshift distribution for the related apparent magnitude. The two vertical dashed lines indicate approximately the locations of the break in the counts at an apparent magnitude of ~ 21 and the PEARLS magnitude limit at an apparent magnitude of ~ 28 . The objects responsible for the shape of the counts reside at relatively low redshifts as indicated by the solid lines ($z \lesssim 2$).

their relative standard deviation: $\bar{\phi}_* = (9.7 \pm 1.8) \times 10^{-3}$, $\bar{M}_* = -20.5 \pm 0.2$, and $\bar{\alpha} = -1.05 \pm 0.09$. The study of traditional LFs can be very informative for trying to understand galaxy evolution. However, here we are trying instead to understand the galaxy number counts, which are plotted in terms of apparent magnitudes. Apparent magnitudes are immediately available from observations, are model independent, and do not require a redshift measurement. On the other hand, rest-frame absolute magnitudes are immediately available from simulations, and here we will use them as a tool to understand how number counts are connected to their constituent LFs.

The right panel of Figure 2 plots the LFs in an unconventional way which represents an intermediate step in converting a set of standard LFs (left panel of Figure 2) into number counts (Figure 1). The conversion of the x -axis, when converting the LFs from the traditional view in the left panel to the unconventional view in the right panel of Figure 2, is from rest-frame absolute magnitudes into observer-frame apparent magnitudes. This conversion shifts the LFs due to two main effects. The first effect is the band shifting due to redshifting of photons. Emitted photons with frequency ν at redshift z have a lower-frequency ν_o when reaching the observer frame. If the spectra of galaxies were completely flat, the flux at ν_o and the flux at ν would be the same. Since this is not the case, to model this effect we need to know the shape of the spectrum to know the value of the flux both at ν_o and at ν , so that we can correct the flux by their ratio. We refer to this as k -correction. The second effect is the decrease in flux as objects move farther away. The dimming effect moves the LFs toward fainter apparent magnitudes (moving to the right), while the band shifting can increase (moving to the left) or decrease (moving to the right) the flux based on the shape of the SED. Hence, while the dimming effect applies rigidly to all LFs in every filter, band shifting can have a different effect on the LF based on the filter being used. This is because at different redshifts we are looking at different parts of the SED, and this can affect how the LFs move in different filters when looking at different redshifts.

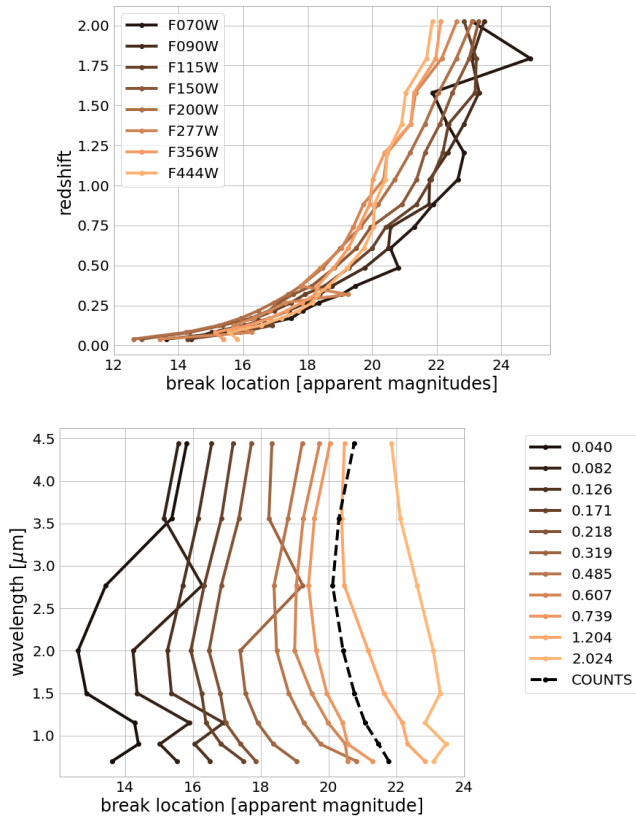


Figure 4. Apparent magnitudes of the break in the power law for different LFs as a function of redshift (top panel) and wavelength (bottom panel).

The conversion for the y-axis to connect the LFs to the number counts needs to take into account the change in the number of galaxies when moving from a simulated box to an area of the sky. When considering a classic LF, we plot the number of objects per unit comoving volume per magnitude bin. However, when we compute the number counts we have the number of objects per unit area. This means that we need to take into account the fact that for a fixed area on the sky, we have a volume element which itself is a function of redshift. The change in the volume element depends on the underlying cosmology, defined by the components of the energy density of the Universe, i.e., matter, Ω_m (including both baryons and dark matter), and dark energy, Ω_Λ .²³ Assuming the standard values for the cosmological parameters as measured by Planck (Planck Collaboration et al. 2014), up to about $z \sim 2.5$ the comoving volume increases with redshift. This means that the number of objects gets boosted with increasing redshift when LFs are considered per unit observed area on the sky rather than per unit volume. In principle, the LFs plotted this way would be shifted down in amplitude for redshifts higher than $z \sim 2.5$ (as the element of comoving volume starts to decrease). This is an additional reason why higher-redshift LFs do not affect the shape of the counts. When translating the number of objects per unit volume into the number of objects per unit area, we obtain the LFs with the same y-axis units as the number counts. This is what we get in the right panel of Figure 2. The additional step that is needed to convert the set of LFs in these new units into number counts is an integration

²³ Usually the energy density of radiation, Ω_γ , and curvature Ω_k , can be neglected.

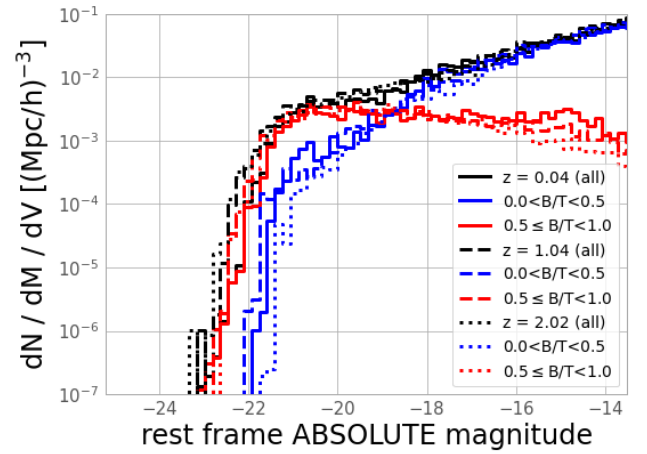


Figure 5. The predicted LFs in the F444W filter at three redshift outputs as indicated by the key. The different colors indicate different morphologies as classified by the B/T criterion (see text). The similarities of the three LFs plotted indicate that the intrinsic properties of galaxies vary less than the cosmological evolution of observed properties due to redshift (i.e., the LFs in the left panel of Figure 2, plotted in terms of rest-frame magnitude, vary less than those in the right panel, plotted against observed magnitude). The contribution of high and low B/T to the LF is the same at each redshift. This means bulge-dominated galaxies dominate the bright part of the LF and disk-dominated galaxies contribute to the faint part of the LF.

over redshift. This is exactly what has been done to obtain the GALFORM number counts in Figure 1.

Given the fact that the integration over all the LFs in the right panel of Figure 2 gives the number counts, we can consider the highest curve as the one making the dominant contribution. Moreover, since the outputs of the simulation are enough to sample very well the redshift range studied, we can imagine a line connecting the highest point of the rescaled LFs at each apparent magnitude and see how this shows the same break at around magnitude $m_{AB} \sim 21$. We decided to plot LF curves only for the F444W filter as this is the one with the most pronounced break, but the simulation accurately reproduces a softer break for the other shorter-wavelength filters as is seen in the PEARLS observations (see Figure Set 2 in the online version to compare the constituent LFs in units of number counts for all the filters). This can be explained by what we can call a compression of the LFs. By this, we mean that the LFs are spread over a certain range of apparent magnitudes. This range is wider for a shorter-wavelength filter like F090W, and narrower for a longer-wavelength filter like F444W. By looking at the intermediate filters as well, this effect is readily apparent: going from $0.9 \mu m$ to $\sim 2 \mu m$, the LFs get brighter for all the redshift outputs plotted in Figure 2 (preserving approximately the range of apparent magnitude covered). However, between the F200W and F277W filters, some low-redshift LFs start to get fainter while the higher-redshift LFs keep getting brighter; this effect gets stronger going from the F277W to F444 filters, creating the compression effect just mentioned, which diminishes the range of apparent magnitudes covered (compare the figures in Figure Set 2, available in the online version). This is the combined effect of the band shifting and dimming created by redshift. In fact, while the dimming effect always decreases the flux with increasing redshift, the band shifting can increase or decrease the flux depending on whether we are climbing or descending the SED (see more in Section 3.6). Whether the dimming effect and the band shifting are contributing together in

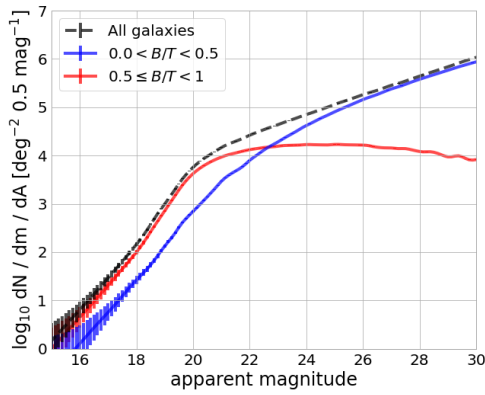


Figure 6. Simulated galaxy number counts in the NIRCам F444W filter, and relative Poisson uncertainty. Different line colors are used to indicate morphology through the B/T proxy, as shown by the legend. The black dashed line is for all objects. The blue line is for disk-dominated galaxies with $B/T \leq 0.5$. The red line shows bulge-dominated galaxies with $B/T \geq 0.5$. It is clear that bulge-dominated galaxies make up the bright part of the counts, while disk-dominated galaxies dominate the faint counts. To fully understand the behavior of the counts, this figure can be compared with the redshift distributions of the same objects in Figure 7.

decreasing the flux or contrasting with each other at a specific redshift will result in the LF getting brighter or fainter, leading to the compression effect and hence a stronger break. From Figure 3 it is also clear that different filters track different redshifts, exacerbating the effect just explained. It is also interesting that objects observed by F444W filter change redshift quite rapidly around magnitude ~ 20 – 21 , which corresponds to where the location of the knee in the counts is.

To fully exploit the power of the simulations, in Figure 4 we compare the location of the break of the LFs at different redshift outputs with the location of the break in the galaxy number counts. This is helpful for identifying which redshift is dominating the apparent magnitude of the break in the number counts. In the top panel, we have the apparent magnitude of the break of the LF as a function of redshift (color-coded by the filter). From Figure 1, we know that the break in the counts lies at ~ 21 apparent magnitudes. This is roughly covered by the LFs between redshifts 0.75 and 1.00. This can also be seen in the bottom panel of Figure 4, where we plot again the location of the break of the LFs as a function of wavelength and color-coded by the redshift. The location of the break in the number counts is drawn with a black dashed line, and lies between the LFs at $z = 0.739$ and $z = 1.204$, confirming that this is approximately the redshift range dominating the number counts.

3.3. Which Galaxies Dominate the Number Counts?

To test whether the break in the counts corresponds to a change in the underlying population of galaxies tracked by a specific filter, we decided to look at how different morphologies contribute to the LFs and hence the galaxy number counts. We take a simple approach of using the bulge-to-total stellar mass ratio, denoted by B/T , as a proxy for morphology. We put the threshold at $B/T = 0.5$ so that we can include all the galaxies, and consider galaxies with $B/T < 0.5$ as disk-dominated and those $B/T \geq 0.5$ as bulge-dominated. We stress that the choice of $B/T = 0.5$ as a threshold is robust, as we tested stricter choices such as defining bulge-dominated galaxies as $B/T > 0.75$ and disk-dominated galaxies as

$B/T < 0.25$ and found the same behavior in all the tests with the only difference of not being complete.

Figure 5 shows LFs in three representative outputs of the simulation, i.e., $z = 0.04$, $z = 1.04$, and $z = 2.02$, for the NIRCам F444W filter. As suggested by the left panel of Figure 2, the rest-frame standard LFs do not change much within the redshift range under consideration ($0 < z < 2$), which is the redshift range of the galaxies dominating the number counts (see Figure 3). Figure 5 confirms the self-similar behavior of the LFs also in terms of populations. It is clear that bulge-dominated galaxies dominate the bright part of the LF, while disk-dominated galaxies dominate the faint part. Thus, we can loosely treat the single LF at $z = 0.04$ as being representative of all the others. While doing this, we do not want to ignore the effect of the evolution of intrinsic galaxy properties, but we acknowledge that this effect is negligible in shaping the number counts when compared to the cosmological evolution due to redshift. This is in agreement with J. H. Marr (2023). The interesting feature is that the transition between bulge- and disk-dominated galaxies, in dominating the number of galaxies of the LF, is approximately where the break occurs between the two power laws. We note that in Figure 5 we are only looking at three single LFs, and how this converts into number counts is not trivial. In fact, we need to integrate over the LFs at all redshifts to obtain the number counts. We do this separately for the two populations, and the results are shown in Figure 6.

The black dashed line in Figure 6 corresponds to the GALFORM prediction as plotted in Figure 1, but now we can see the contribution of the two populations of galaxies, i.e., bulge dominated (red line) and disk dominated (blue line). How the integration of the single LFs leads to this shape for the number counts can be seen in the right panel of Figure 2. The combination of the change in comoving volume for a fixed area of the sky and the dimming and band shifting of the objects due to redshift gives a shape to the counts with a well-defined break in power-law slope. In addition, we see in Figure 6 how the different contributions of bulge- and disk-dominated galaxies can describe this broken power law. In fact, the apparent magnitude of the break corresponds to the change in the dominant population, with bulge-dominated galaxies dominating the bright part and disk-dominated galaxies dominating the faint end. Although this is a simple picture, there is an underlying complexity relating to which redshifts contribute the most at each apparent magnitude. In fact, we stress that number counts include objects at all redshifts. To investigate this further, we drew the redshift distribution for two representative apparent magnitude limits (i.e., considering all the objects brighter than the stated limit).

In Figure 7, we plot the redshift distribution for a bright magnitude limit of 23 and a fainter magnitude limit of 28 (which corresponds to the PEARLS sample limit). The first thing to notice is how in both panels the peak of the redshift distribution is limited to relatively low redshifts in the range $1 < z < 2$. The second immediately evident fact is that when considering the bright limit (left panel), bulge objects are dominant in number while the overall trend is inverted when considering the faint limit (right panel). Another more subtle feature is that the peak in the $n(z)$ of the bulge-dominated galaxies is always slightly higher in redshift than for disk-dominated galaxies. This is in agreement with the fact that bulge-dominated galaxies have bigger stellar masses than disk

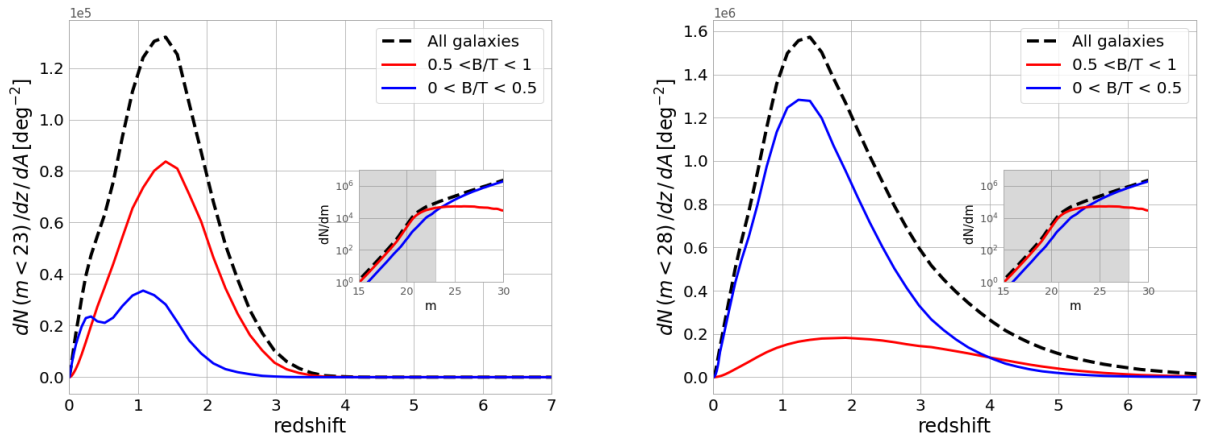


Figure 7. Redshift distributions for the objects plotted in Figure 6. Different colors represent different morphologies according to the B/T criterion as in Figure 6 (see text for a full description). The two panels show the distributions for different magnitude limits. Left: $F444W < 23$. Right: $F444W < 28$ (corresponding to the PEARLS magnitude limit). Bulge-dominated objects dominate the bright counts at most redshifts, while disk-dominated objects dominate the faint counts. Note that the number of galaxies satisfying the brighter limit (left panel) is ~ 1 order of magnitude lower than the number of galaxies satisfying the fainter limit (right panel). The shaded area in the insets helps identify which part of the number counts the galaxies in the redshift distribution belong to.

galaxies and hence are intrinsically brighter. This makes them still visible at higher redshifts when disk galaxies would be already too faint to be seen. In addition to this, there could be another selection effect playing a role. Since we are looking at galaxies mainly below a redshift of 2, with the F444W filter we are looking at rest-frame wavelengths ranging from $4.44 \mu\text{m}$ to approximately $1.48 \mu\text{m}$. These wavelengths are more sensitive to older stellar populations, favoring the observation of bulge-dominated systems.

3.4. Contribution of Bulge-dominated Galaxies

We now focus on the contribution of bulge-dominated galaxies to the counts. The reason for this is that in these galaxies, the change in star formation activity is less dramatic than in disk-dominated galaxies, because of the older stellar populations present in the bulge, facilitating the study of cosmological effects (S. P. Driver et al. 1996). For these galaxies, we consider the number counts after applying a selection on their rest-frame absolute magnitude. The reason for this can be seen in the left panel of Figure 2. When looking at the LFs in the rest frame (left panel of Figure 2), we can think of them as all having approximately the same shape in the redshift range of interest (see the parameters for the Schechter fit performed in Section 3.2). There is little variation in the bright end, due to galaxy evolution (presumably the activity of AGN feedback on massive galaxies). However, this variation is negligible when compared to the variation that LFs have against their observed magnitude. Moreover, we have noted that all the LFs in the redshift range of interest have the same behavior when split by morphology, i.e., bulge-dominated galaxies dominate the bright end and disk-dominated galaxies dominate the faint end (see Figure 5). This implies that if we select galaxies brighter than a given rest-frame absolute magnitude, and vary this selection, then we are progressively sampling a different galaxy population. When the rest-frame absolute magnitude limit is bright, the population is mainly made up of bulge-dominated galaxies. When the limit is at fainter rest-frame absolute magnitudes instead, the population includes both bulge- and disk-dominated galaxies.

In the left panel of Figure 8, we show the counts for six representative rest-frame absolute cuts between -23 (probing the bright end) and -16 (deep into the faint end). The part of the LF these limits are tracking can be seen by examining Figure 5. If we look for example at the brighter limit of $M < -23$, we are selecting only the very bright part of the LF where the high-luminosity bulge-dominated galaxies are the most numerous. Looking at the left panel of Figure 8, we note that these very bright objects are not responsible for the bright apparent magnitudes in the number counts, but they are mostly located at the position of the break in the counts. If we allow the rest-frame absolute magnitude limit to sample slightly fainter objects, we can see that we need those objects to get closer to the total counts. For example, with a limit of $M < -21$, we are getting close to the total number of objects in the counts. A rest-frame absolute magnitude limit of $M < -21$ corresponds roughly to the break in the rest-frame LF as shown in Figure 5. This means that we need all the objects brighter than the break of the LF to reproduce the break in the number counts. For fainter magnitudes than the break in the number counts, we really need the disk galaxies to recover the overall shape of the counts. By using only bulge-dominated galaxies, we note that by taking galaxies with increasingly fainter rest-frame absolute magnitude limits, we can see the cutoff in the number counts moving to fainter apparent magnitudes. In the right panel of Figure 8, we can see the relative redshift distributions on a logarithmic scale, for an apparent magnitude limit of 28. We have already seen that for the total counts, we expect the mean of the redshift distribution to be below $z \sim 2$. Here, we can see what the whole redshift distribution for bulge-dominated galaxies looks like and the difference when we include only intrinsically luminous objects and all the galaxies up to a faint limit. Given the field of view of NIRCcam, we expect to have one object per field of view when the y-axis is $\sim 7 \times 10^{-2} \frac{\text{galaxies}}{\text{deg}^2}$ (dashed horizontal line on the right side of Figure 8). Hence, when compared to the observations from NIRCcam, it makes sense to only consider the counts above that threshold. It is interesting to note that when we consider objects more luminous than an absolute magnitude of -21 , we are almost considering all the bulge-dominated galaxies that have an effect in shaping the number

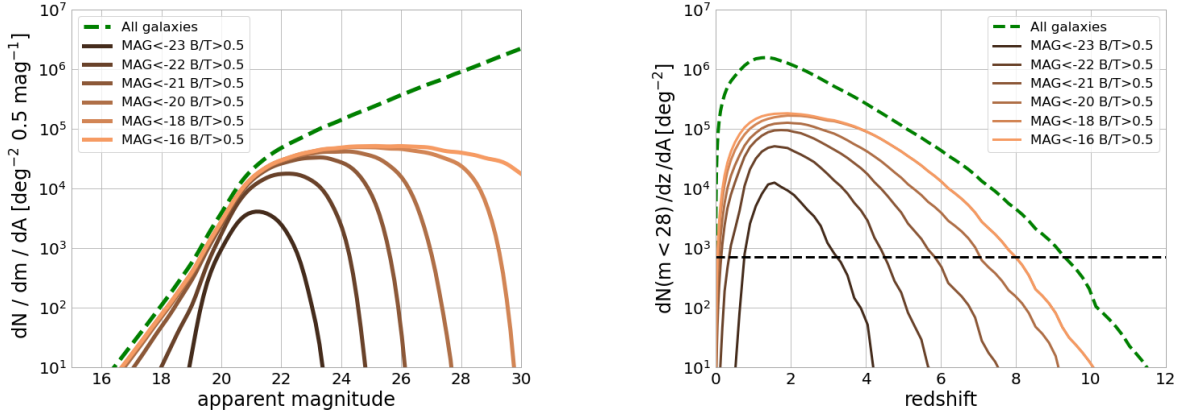


Figure 8. Left: simulated galaxy number counts in the F444W filter, built by using the LFs of objects satisfying different criteria, indicated by the line color, where dashed green denotes all objects, and all other lines are for objects with a bulge-to-total mass ratio greater than 0.5 ($B/T \geq 0.5$), selecting bulge-dominated galaxies. Apart from the dashed green line, all the other lines only use objects with a rest-frame absolute magnitude brighter than the threshold indicated in the legend. Right: redshift distribution in logarithmic units (on the y-axis) for the same objects in the left plot when applying an apparent magnitude limit of F444W < 28. The dashed horizontal black line indicates the limit of one object per NIRCcam field of view.

counts. In fact, the number counts already look almost complete at the bright end when using that magnitude limit. One final remark is that although the redshift distribution on the right side of Figure 8 seems to show a substantial number of galaxies at redshift higher than 2, the mean value of the distribution is always below that redshift even when ignoring the contribution of the disk galaxies, which would lower the mean of the redshift distribution to lower redshifts. Moreover, when plotting the distribution on a linear scale, it is clearly visible how small the contribution of bulge-dominated galaxies is compared to disk galaxies when considering a faint apparent magnitude limit of 28. In fact, the horizontal dashed line on the right panel of this figure corresponds to one object per field of view. This is the reason why we can easily reconstruct the number counts by using LFs with redshifts lower than 2.

3.5. Contribution of Different Stellar Masses

A further piece of information that can help in understanding the shape of the number counts comes from the stellar masses of galaxies. The question we want to address in Figure 9 is which stellar masses are contributing at different apparent magnitudes to the number counts. A further question is if this contribution differs significantly in different NIRCcam filters, i.e., if there is a wavelength dependence. It is worth clarifying that since we are dealing with a semi-analytical model, rather than observed data, stellar masses are directly derived from physical processes which combine galaxy formation (e.g., gas cooling, feedback processes, metallicities) with the hierarchical evolution of dark matter halos. To obtain luminosities, mass-to-light ratios are computed on a per-object basis, based on the star formation and chemical evolution histories predicted for each galaxy. In the top row of Figure 9, we show the number counts for the shorter (F090W) and longer (F444W) NIRCcam filters available in the PEARLS observations used here. The overall counts (green dashed line) are then split into different mass bins 1 dex wide and ranging from 10^5 to $10^{12} M_\odot$. This figure is somewhat related to Figure 8 as absolute magnitudes are, to an extent (depending on the wavelength), related to stellar masses (more massive galaxies tend to be more luminous). In fact, we can see that the most massive galaxies, those with stellar masses between $10^{11} < M_*/M_\odot < 10^{12}$, are not those that contribute the most

to the bright end of the counts but instead galaxies between $10^{10} < M_*/M_\odot < 10^{11}$ are dominant. This is in agreement with what we see in Figure 8, where the brightest galaxies ($M_{AB} < -23$) are not able alone to fully populate the bright end as lower-luminosity galaxies (approximately $M_{AB} < -21$) need to be taken into account to fully reproduce the bright end of the counts. By comparing the two panels in the top row of Figure 9, it is interesting how the contributions of different stellar masses are different when comparing the shorter-wavelength filter at $0.90 \mu\text{m}$ (left panel) with the longer-wavelength filter at $4.44 \mu\text{m}$ (right panel). In the F090W filter, we can see that the contribution of different stellar masses spreads over a wide range of apparent magnitudes with a smooth profile that is reflected in a weak break in the slope of the overall counts. The knee in the counts for the F444W filter is definitely more pronounced, as the contributions to the counts from the stellar-mass-selected samples are more peaked. Moreover, it is clear how the bright part of the counts, brighter than the break, is mainly constituted by galaxies with stellar masses bigger than $10^{10} M_\odot$. The last thing to note is that this simulation has been built with a dark matter halo mass resolution of $10^{8.5} M_\odot$, which for this model translates to a stellar mass resolution of $\sim 10^5 M_\odot$. However, from the top row of Figure 9, we can see that galaxies with stellar masses below $10^6 M_\odot$ are not important in shaping the number counts as they would be a very tiny number with an observational magnitude limit of $m = 28$. In the lower panels of Figure 9, we see the corresponding redshift distributions, using the same color-coding as for the stellar mass bins. It can be seen that although the counts in the shorter-wavelength filter have a broader distribution in apparent magnitude, the corresponding redshift distributions are more peaked than is the case with the longer-wavelength filter. This shows how the relative shift of the single LFs between themselves is more important than the overall shift of the LFs due to cosmological dimming when interpreting the shape of the number counts. We devote the following section to an explanation of this statement.

3.6. Relation between SED and Number Counts

To understand the origin of the break in the number counts and why the change in slope is more pronounced at different

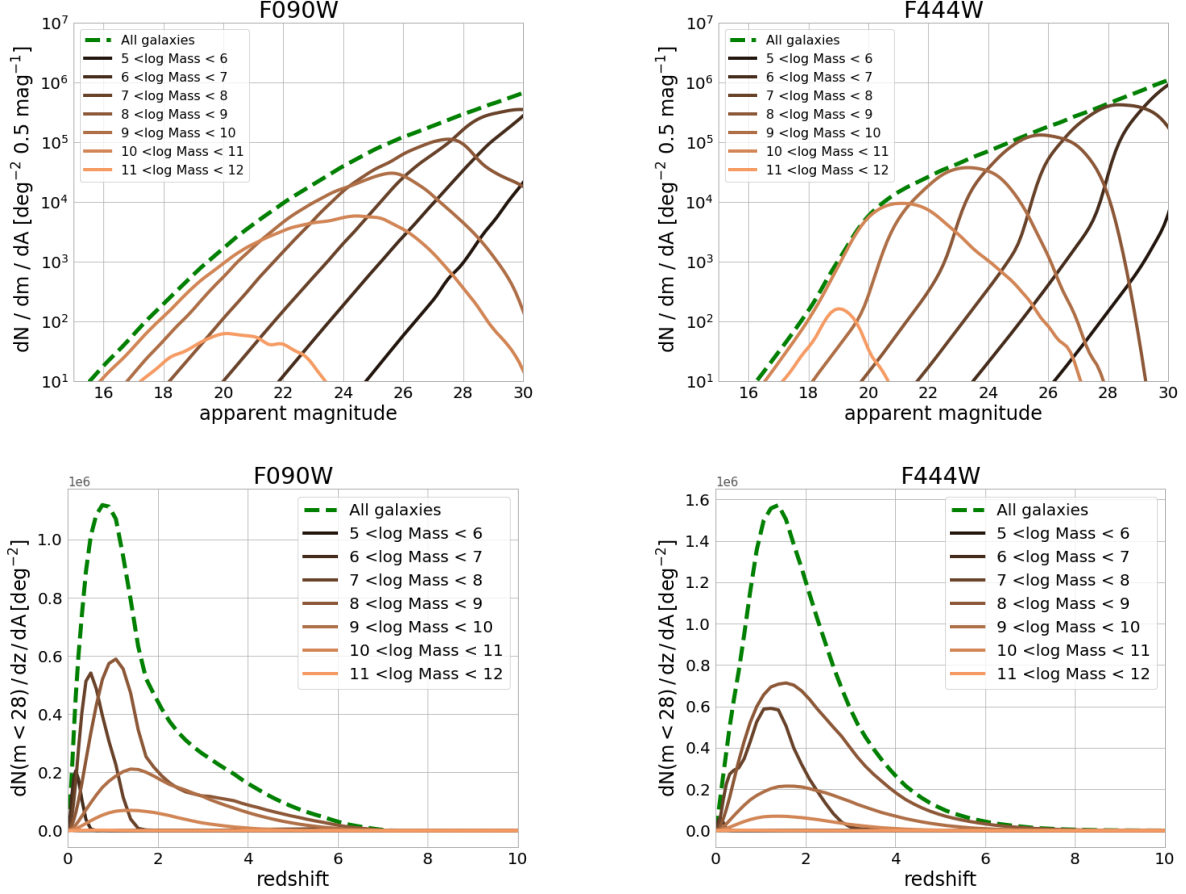


Figure 9. Galaxy number counts (top row) and relative redshift distributions (bottom row) split in bins of stellar mass to study the contribution of each stellar mass bin to each apparent magnitude. The analysis is repeated for the shortest-wavelength NIRCcam filter available in PEARLS, F090W (left column), and the longest-wavelength, F444W (right column). The green dashed line in all panels includes all the simulated objects, while other colors show the contribution of different stellar mass bins.

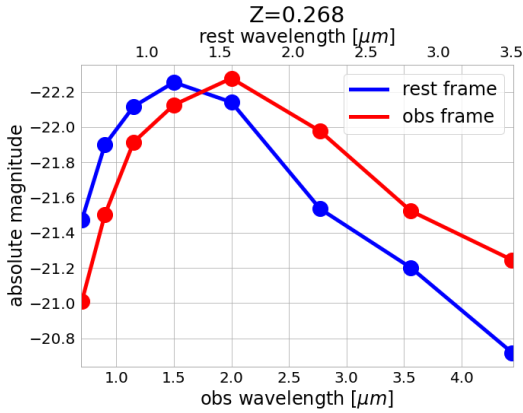


Figure 10. Comparison between the observer-frame (red line) and rest-frame (blue line) SEDs of a galaxy at $z = 0.268$. This figure shows how band shifting of the SED can create a decrease in flux at the wavelengths before the crossover (positive k -correction) and an increase in flux for longer wavelengths (negative k -correction). The example galaxy was chosen to have a B/T close to 1, in order to sample a bulge-dominated galaxy.

wavelengths, it is important to understand how the region of the SED sampled changes as photons travel from the rest frame of the galaxy to the telescope (the observer frame). It is clear from Figure 2 that the conversion between rest frame (left panel) and observer frame (right panel) is the cause of the

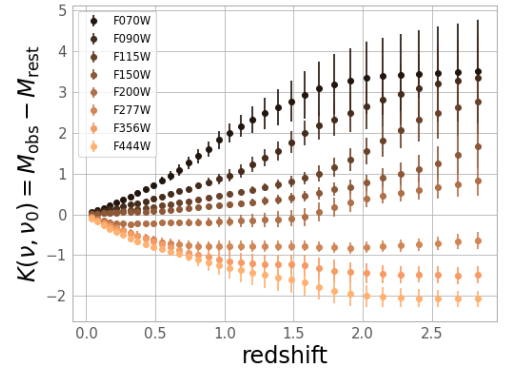


Figure 11. Frequency part of the k -correction as a function of redshift for all the wide NIRCcam filters; see Equation (1). The points represent the median, and the error bars represent the standard deviation over the simulated sample at different snapshots.

spread in the LFs with redshift, and hence the break in the counts slope. The reason why the break depends on the observed wavelength of the counts is related to the shape of the SED and its transition from the rest frame to the observer frame. The k -correction quantifies the transformation between the rest and observer frames. Details on how to derive the equations for the k -correction can be found in textbooks such as M. S. Longair (2023); we limit ourselves here to reporting

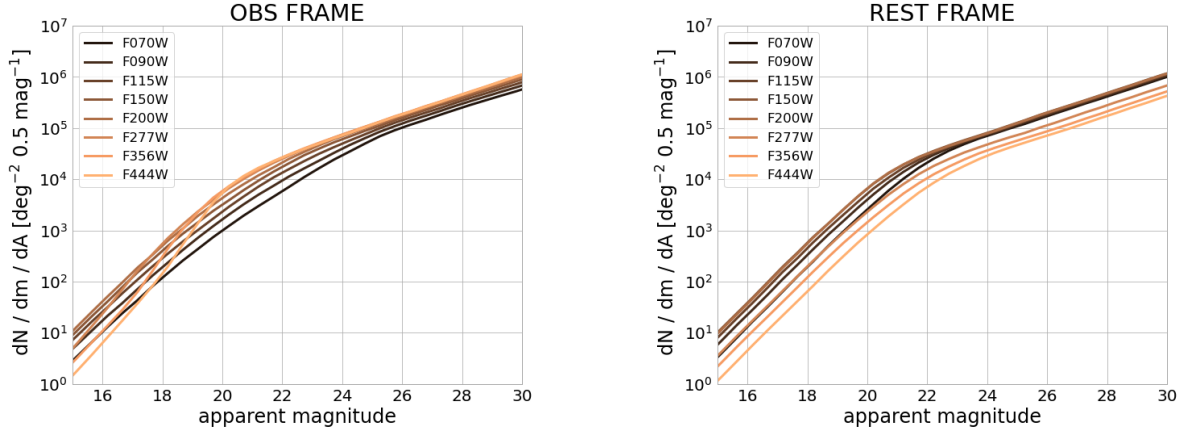


Figure 12. Galaxy number counts in the observer frame (left panel) and rest frame (right panel) for all the wide NIRCam filters.

the convention used in GALFORM:

$$\mathcal{K} = -2.5 \log_{10}(1 + z) - 2.5 \log_{10} \left(\frac{L_{\nu}}{L_{\nu_0}} \right), \quad (1)$$

with L_{ν} being the luminosity at the emitted wavelength and L_{ν_0} the luminosity at the observed wavelength.²⁴ The first term represents the stretch of the spectrum with redshift (bandpass stretch correction), while the second term takes into account the difference in the spectrum at the emitted and observed wavelengths. The second term of the k -correction, which depends only on wavelength and not on redshift, can also be expressed as $M_{\text{obs}} - M_{\text{rest}}$. This is very important as here we want to show that the feature responsible for the change in the intensity of the break in the counts, for different filters, is the frequency part of the k -correction, i.e., the second term of Equation (1), when applied to the infrared SED of a galaxy. The advantage of using the GALFORM simulations is that we have access to both M_{rest} and M_{obs} . This is something that is not possible by using only observational data. In the unrealistic case in which the SED of a galaxy were flat (i.e., the same intensity at all wavelengths), the intrinsic luminosity of a galaxy would be the same in the rest and observer frames, and there would be no difference between M_{rest} and M_{obs} . However, for any SED with an intrinsic shape, the luminosity L_{ν} will always be different from L_{ν_0} , as we are probing different parts of the SED. The way GALFORM computes SEDs is the following. It computes the mass-to-light ratios in a set of filters specified at a run time, rather than storing the SED for each galaxy. The SEDs for stellar populations of a single age and metallicity are converted into the corresponding mass-to-light ratio. This is done for the full grid of ages and metallicities supplied by the stellar population synthesis (SPS) models, so that these results can be used to build the mass-to-light ratio in a specified filter for a composite stellar population. A filter can be specified in both the rest frame and observer frame (which is redshift dependent), and so the k -correction can be calculated exactly on a galaxy-by-galaxy

basis at the output redshifts used in the model. In this work, we used SPS models from C. Maraston (2005).

We now use Figure 10 to understand how the frequency part of the k -correction can give rise to the break in the number counts. In this figure, we plot M_{obs} with a red line and M_{rest} with a blue line as a function of frequency for an example galaxy at $z = 0.268$.

The key point is that the transformation between rest and observer frames is the only wavelength-dependent part when converting LFs to number counts, hence only it could be the reason for the differences in the break strength at different filters.

At $z = 0$, the observer- and rest-frame SEDs would overlap, but as redshift increases, the observer-frame SED would shift to longer wavelengths than the one covered by the filters. This requires a theoretical model to know what the SED would look like in the wavelengths not sampled. Figure 10 shows that at shorter wavelengths of the crossing points between rest- and observer-frame SEDs, we observe a decrease in flux, while at longer wavelengths the galaxy receives a boost in flux. This is purely due to the k -correction and plays a crucial role in shaping the number counts at different wavelengths. In fact, this is what indirectly makes the break in the number counts more or less pronounced in different filters.

In Figure 11, we plot the k -correction as a function of redshift. This is to show that for the same filter at different redshifts, the k -correction may be very different. This is crucial for interpreting the break in the counts, as it creates a “compression” of the observer-frame LFs at the position of the break. Integrating the observer-frame LFs at all redshifts to get the number counts contributes to shaping the strength of the break.

It is important to clarify that although the k -correction plays a crucial role in shaping the break of the power law in the number counts, it is not the only reason for the break. To verify this, we plot the standard number counts in the observer frame in the left panel of Figure 12, together with the number counts in the rest frame as they would appear without taking into consideration the effect of the k -correction in the right panel.

We find that the break will still be in the counts as a result of the break in the constituent LFs, however the break will look the same in all the filters. When negative, the k -correction makes the breaks more pronounced; when positive, it makes the break shallower. This is more obvious in Figure 13, where

²⁴ This does not include any dimming effect, as this is involved in the conversion between apparent and absolute magnitude. Here we just include the luminosity from the spectrum at different wavelengths (rest and observed).

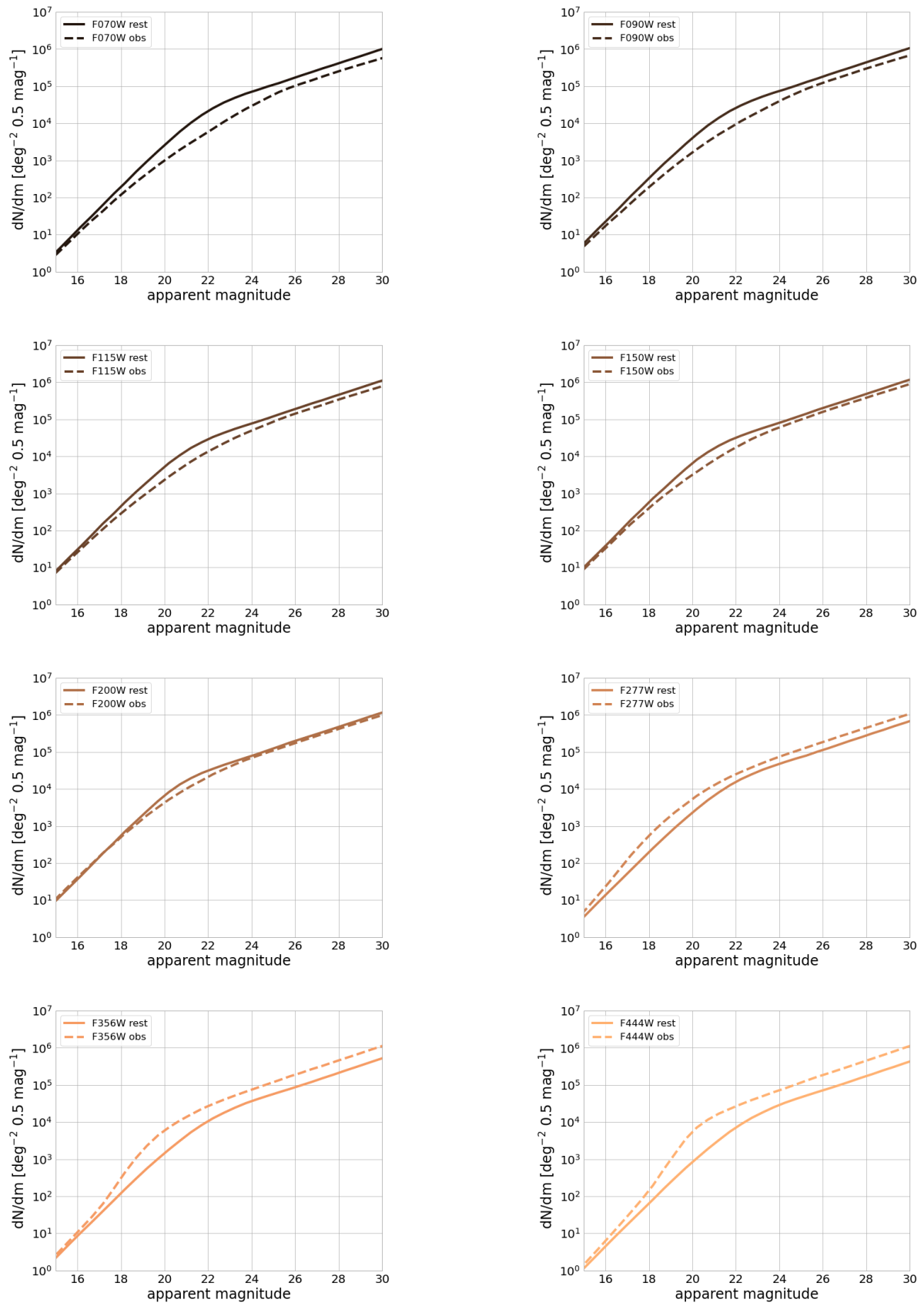


Figure 13. Comparison between the number counts in the observer frame and in the rest frame to study the effect of the change in reference frame controlled by the k -correction.

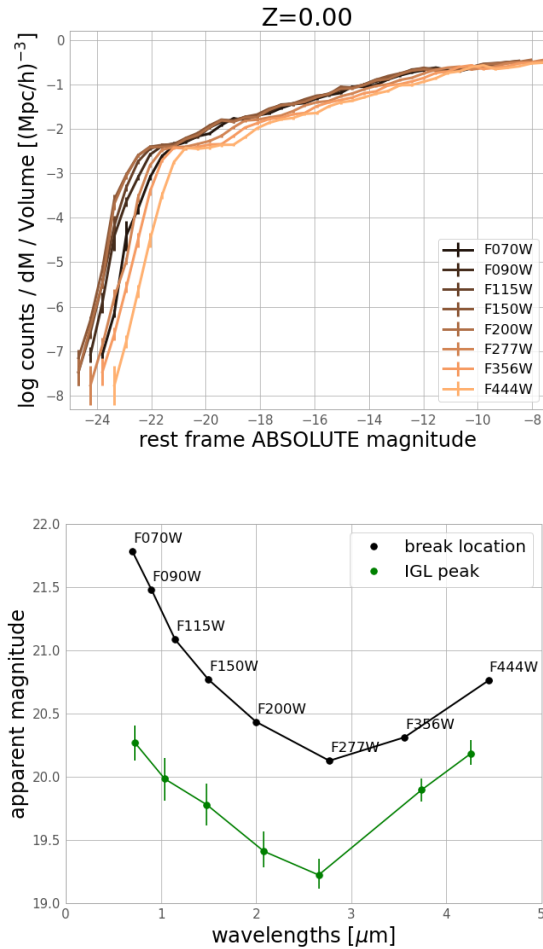


Figure 14. Top panel: LFs in rest-frame absolute magnitudes at $z = 0$ for all the NIRCcam wide filters. The intrinsic luminosity of the galaxies varies depending on the filter, with a peak between F150W and F200W. This corresponds to the peak of the integrated galaxy light (IGL) and, as a consequence, to the brightest break in the number counts. Bottom panel: apparent magnitude of the break in the number counts as a function of wavelength (black line). The trend is a consequence of the intrinsic luminosity of the LFs in the top panel. The same trend is seen in the IGL, with a peak at around 2–3 μm .

we plot each filter in a different panel to compare the difference in the observer and rest frames.

As anticipated in Section 3.1, the slope of the bright end of the observed counts changes significantly, while the slope of the faint end remains almost constant; we report in Table 1 the values of the fits to the GALFORM prediction, with their standard errors.²⁵

Another feature noticeable from the right panel of Figure 12 is that counts in the rest frame get brighter from F070W to F200W, and then fainter again from F200W to F444W. Since we are looking in the rest frame, this has to be related to the intrinsic luminosity of the galaxies. In the top panel of Figure 14, we plot the LFs at $z = 0$ and they follow the same trend, confirming our hypothesis that this behavior is not related to the change of reference frame. As a further test, in the bottom panel of the same figure, we compare the location of the break in the number counts as a function of wavelength to the peak of the integrated galaxy light (IGL) from Figure 11

of R. A. Windhorst et al. (2023). This suggests that both the location of the break and the IGL are driven by the intrinsic luminosity of the galaxies. However, the strength of the break is a result of the change in the k -correction with redshift.

A final remark is that although this effect has never been studied in detail to justify the shape of the infrared galaxy number counts, in submillimeter galaxies the boost in flux due to a negative k -correction is a well-known phenomenon (see, e.g., A. W. Blain & M. S. Longair 1993). In fact, A. W. Blain & M. S. Longair (1993) showed that the extent of the k -correction at high redshift in the submillimeter window could be so large (and negative, i.e., a boost in the observed flux) that it can make visible galaxies that are too faint to be observed in rest-frame wavelengths.

4. Conclusions

We have taken advantage of the incredible depth of JWST observations from R. A. Windhorst et al. (2023) to develop a deeper understanding of the double power law that is clearly present in the NIRCcam galaxy number counts, ranging from 0.7 μm to 4.4 μm . The change in slope is more pronounced at longer wavelengths than at shorter wavelengths. We made use of the GALFORM semi-analytical model to understand the origin of the break. The model is able to reproduce the JWST counts in all of the filters, reproducing the location of the change in slope and the strength of the break quite accurately (see Figure 1 with the associated Figure Set 1 available online; see also the GALFORM predictions for JWST in W. I. Cowley et al. 2018; S. Lu et al. 2025). This means that the physics responsible for the break in the counts is included in the model, suggesting that we are not going to uncover new galaxy formation physics purely through the study of the number counts. We split the analysis of the counts into LFs, and found (see Figure 3) that the redshifts of the LFs dominating the counts are relatively low ($z \lesssim 2$) when limiting our model to the observational magnitude cut of ~ 28 (as in the PEARLS observations in R. A. Windhorst et al. 2023). This rules out the possibility of using the galaxy number count to infer strong constraints on the early Universe, as for this magnitude limit the galaxies shaping the counts are those at low and intermediate redshifts. By studying the contributions of individual LFs in the outputs of the simulation at instantaneous snapshots, we were able to uncover the origin of the break and why it changes strength with wavelength. The break in the galaxy number counts does not arise due to a particular physical process or anything related to structure formation (other than the physics defining the break in the LF), but is an observational effect due to the fact that the number counts are defined in the observer frame and not in the rest frame like the LF. When looking at the LFs contributing to the counts in the rest frame, we note that they are all self-similar apart from a small contribution due to the intrinsic evolution of galaxies and the change in star formation (see left panel of Figure 2). However, when we look at the LFs in the observer frame (right panel of Figure 2), for a given filter the k -correction contributes in different ways at different redshifts, creating a “compression” at the location of the break. The reason for this is the intrinsic shape of the SED and the resulting k -correction, which for a fixed redshift can be either positive (a decrease in flux) or negative (an increase in flux), depending on the filter used. To better understand this process, we took an example of a GALFORM-simulated galaxy and compared the rest-frame

²⁵ Note that the tiny errors are due to the large statistics of our simulation and the associated small Poisson errors.

and observer-frame SEDs (Figure 10), as the difference between them defines the k -correction. For shorter wavelengths than the intersection between rest- and observer-frame SEDs, the flux in the observer frame will be lower than in the rest frame. For longer wavelengths, the flux will receive a boost when converting from the rest frame to the observer frame. The location of the intersection between observer- and rest-frame SEDs differs with redshift as the k -correction is different. This means that a LF in a specific filter will move to brighter or fainter magnitudes depending on the boost or decrease in flux regulated by a positive or negative k -correction.

For the first time here, we use the effect on the flux of a positive/negative k -correction to explain the shape of the near-infrared number counts and the clear knee as observed by JWST's NIRCam. This work proves the importance of the change in reference frame in interpreting galaxy number counts. It shows the crucial contribution of the k -correction in shaping the break in the number counts and defining its strength. We show that the origin of the break is a combination of different observational effects related to the change in reference frame in an expanding Universe, combined with the break present in the LFs. The role of galaxy evolution in the shape of the constituent LFs is minor compared to the effect of the change in reference frame. We can consider self-similar LFs in the rest frame and still obtain the break in the observed number counts, as shown in Figure 2.

With this work, we put together for the first time a full, consistent, and physically motivated framework to explain the appearance of the number counts in near-infrared deep observations by JWST. Regarding the study of the early Universe using galaxy statistics, we warn the reader that extra care must be taken when dealing with high-redshift faint galaxies as these have no role in defining the shape of the galaxy counts, at least to the observational magnitude limit of $m_{AB} \lesssim 28$. Now that we are fully aware of the observational biases that result from the change in the reference frame, we have set the ground for the use of galaxy formation models to test different dark matter models by changing the underlying dark matter power spectrum.

Acknowledgments



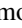
G.M. is supported by the Collaborative Research Fund under grant No. C6017-20G, which is issued by the Research Grants Council of Hong Kong S.A.R. This work used the DiRAC@Durham facility managed by the Institute for Computational Cosmology on behalf of the STFC DiRAC HPC Facility (www.dirac.ac.uk). The equipment was funded by BEIS capital funding via STFC capital grant Nos. ST/K00042X/1, ST/P002293/1, ST/R002371/1 and ST/S002502/1, Durham University, and STFC operations grant No. ST/R000832/1. DiRAC is part of the National e-Infrastructure. This work is based on observations made with the NASA/ESA/CSA James Webb Space Telescope. The data were obtained from the Mikulski Archive for Space Telescopes at the Space Telescope Science Institute, which is operated by the Association of Universities for Research in Astronomy, Inc., under NASA contract NAS 5-03127 for JWST. These observations are associated with JWST programs 1176 and 2738.

Data Availability

The data that support the findings of this study are stored at the Durham COSMA facilities. Please contact the corresponding author to have access. The JWST fields, used by R. A. Windhorst et al. (2023) to obtain the observed number counts, are available at doi:10.17909/z0aj-zm13 for IDF-epoch1 and doi:10.17909/mw1y-gb32 for El Gordo.

Facility: MAST.

ORCID iDs

Giorgio Manzoni  <https://orcid.org/0000-0001-8220-2324>
Tom Broadhurst  <https://orcid.org/0000-0002-8785-8979>
Jeremy Lim  <https://orcid.org/0000-0003-4220-2404>
Tao Liu  <https://orcid.org/0000-0002-5248-5076>
George Smoot  <https://orcid.org/0000-0001-7575-0816>
Carlton M. Baugh  <https://orcid.org/0000-0002-9935-9755>
Scott Tompkins  <https://orcid.org/0000-0001-9052-9837>
Rogier Windhorst  <https://orcid.org/0000-0001-8156-6281>
Simon Driver  <https://orcid.org/0000-0001-9491-7327>
Timothy Carleton  <https://orcid.org/0000-0001-6650-2853>
Brenda Frye  <https://orcid.org/0000-0003-1625-8009>
Leo Fung  <https://orcid.org/0000-0002-5899-3936>
Jiashuo Zhang  <https://orcid.org/0000-0002-3783-4629>
Seth H. Cohen  <https://orcid.org/0000-0003-3329-1337>
Christopher J. Conselice  <https://orcid.org/0000-0003-1949-7638>
Norman A. Grogin  <https://orcid.org/0000-0001-9440-8872>
Rolf A. Jansen  <https://orcid.org/0000-0003-1268-5230>
Anton M. Koekemoer  <https://orcid.org/0000-0002-6610-2048>
Rafael Ortiz, III  <https://orcid.org/0000-0002-6150-833X>
Norbert Pirzkal  <https://orcid.org/0000-0003-3382-5941>
Christopher N. A. Willmer  <https://orcid.org/0000-0001-9262-9997>

References

- Altieri, B., Berta, S., Lutz, D., et al. 2010, *A&A*, **518**, L17
Ashby, M. L. N., Willner, S. P., Fazio, G. G., et al. 2013, *ApJ*, **769**, 80
Baugh, C. M., Gonzalez-Perez, V., Lagos, C. d. P., et al. 2019, *MNRAS*, **483**, 4922
Bertin, E., & Arnouts, S. 1996, *A&AS*, **117**, 393
B  thermin, M., Le Floc'h, E., Ilbert, O., et al. 2012, *A&A*, **542**, A58
Blain, A. W., & Longair, M. S. 1993, *MNRAS*, **264**, 509
Blanton, M. R., & Roweis, S. 2007, *AJ*, **133**, 734
Broadhurst, T. J., Ellis, R. S., & Glazebrook, K. 1992, *Natur*, **355**, 55
Cole, S., Lacey, C. G., Baugh, C. M., & Frenk, C. S. 2000, *MNRAS*, **319**, 168
Coleman, G. D., Wu, C. C., & Weedman, D. W. 1980, *ApJS*, **43**, 393
Cooray, A. 2016, *RSOS*, **3**, 150555
Cowie, L. L., Gardner, J. P., Hu, E. M., et al. 1994, *ApJ*, **434**, 114
Cowie, L. L., Songaila, A., Hu, E. M., & Cohen, J. G. 1996, *AJ*, **112**, 839
Cowley, W. I., Baugh, C. M., Cole, S., Frenk, C. S., & Lacey, C. G. 2018, *MNRAS*, **474**, 2352
Davies, L. J. M., Thorne, J. E., Robotham, A. S. G., et al. 2021, *MNRAS*, **506**, 256
Driver, S. P., Andrews, S. K., Davies, L. J., et al. 2016, *ApJ*, **827**, 108
Driver, S. P., Hill, D. T., Kelvin, L. S., et al. 2011, *MNRAS*, **413**, 971
Driver, S. P., Phillipps, S., Davies, J. I., Morgan, I., & Disney, M. J. 1994, *MNRAS*, **266**, 155
Driver, S. P., Windhorst, R. A., Ostrander, E. J., et al. 1995, *ApJL*, **449**, L23
Driver, S. P., Windhorst, R. A., Phillipps, S., & Bristow, P. D. 1996, *ApJ*, **461**, 525
Elliott, E. J., Baugh, C. M., & Lacey, C. G. 2021, *MNRAS*, **506**, 4011
Gardner, J. P., Cowie, L. L., & Wainscoat, R. J. 1993, *ApJL*, **415**, L9
Gardner, J. P., Sharples, R. M., Carrasco, B. E., & Frenk, C. S. 1996, *MNRAS*, **282**, L1

- Glazebrook, K., Ellis, R., Santiago, B., & Griffiths, R. 1995, *MNRAS*, **275**, L19
- Gruppioni, C., Pozzi, F., Zamorani, G., & Vignali, C. 2011, *MNRAS*, **416**, 70
- Herschel, W. 1785, *RSPT*, **75**, 213
- Hogg, D. W. 1999, arXiv:astro-ph/9905116
- Hubble, E. 1934, *ApJ*, **79**, 8
- Jones, L. R., Fong, R., Shanks, T., Ellis, R. S., & Peterson, B. A. 1991, *MNRAS*, **249**, 481
- Kapteyn, J. C. 1922, *ApJ*, **55**, 302
- Kim, S. J., Goto, T., Ling, C.-T., et al. 2024, *MNRAS*, **527**, 5525
- Koushan, S., Driver, S. P., Bellstedt, S., et al. 2021, *MNRAS*, **503**, 2033
- Lacey, C., & Cole, S. 1993, *MNRAS*, **262**, 627
- Lacey, C. G., Baugh, C. M., Frenk, C. S., et al. 2016, *MNRAS*, **462**, 3854
- Ling, C.-T., Kim, S. J., Wu, C. K. W., et al. 2022, *MNRAS*, **517**, 853
- Longair, M. S. 2023, *Galaxy Formation* (New York: Springer)
- Lu, S., Frenk, C. S., Bose, S., et al. 2025, *MNRAS*, **536**, 1018
- Madar, M., Baugh, C., & Shi, D. 2024, *MNRAS*, **535**, 3324
- Madau, P., & Dickinson, M. 2014, *ARA&A*, **52**, 415
- Madau, P., & Pozzetti, L. 2000, *MNRAS*, **312**, L9
- Manzoni, G., Baugh, C. M., Norberg, P., et al. 2024, *MNRAS*, **530**, 1394
- Maraston, C. 2005, *MNRAS*, **362**, 799
- Marr, J. H. 2023, *Galax*, **11**, 65
- Metcalf, N., Shanks, T., Fong, R., & Jones, L. R. 1991, *MNRAS*, **249**, 498
- Noonan, T. W. 1971, *PASP*, **83**, 31
- Parkinson, H., Cole, S., & Helly, J. 2008, *MNRAS*, **383**, 557
- Planck Collaboration, Ade, P. A. R., Aghanim, N., et al. 2014, *A&A*, **571**, A16
- Robotham, A. S. G., Davies, L. J. M., Driver, S. P., et al. 2018, *MNRAS*, **476**, 3137
- Rowan-Robinson, M. 2024, *MNRAS*, **527**, 10254
- Sajkov, L., Sajina, A., Pope, A., et al. 2024, *ApJ*, **977**, 115
- Sandage, A. 1961, *ApJ*, **133**, 355
- Seares, F. H., van Rhijn, P. J., Joyner, M. C., & Richmond, M. L. 1925, *ApJ*, **62**, 320
- Shanks, T., Stevenson, P. R. F., Fong, R., & MacGillivray, H. T. 1984, *MNRAS*, **206**, 767
- Shapley, H., & Ames, A. 1932, *AnHar*, **88**, 41
- Shupe, D. L., Rowan-Robinson, M., Lonsdale, C. J., et al. 2008, *AJ*, **135**, 1050
- Smail, I., Hogg, D. W., Yan, L., & Cohen, J. G. 1995, *ApJL*, **449**, L105
- Stach, S. M., Smail, I., Swinbank, A. M., et al. 2018, *ApJ*, **860**, 161
- Stone, M. A., Alberts, S., Rieke, G. H., et al. 2024, *ApJ*, **972**, 62
- Tinsley, B. M. 1977, *ApJ*, **211**, 621
- Tinsley, B. M. 1980, *ApJ*, **241**, 41
- Windhorst, R. A., Cohen, S. H., Hathi, N. P., et al. 2011, *ApJS*, **193**, 27
- Windhorst, R. A., Cohen, S. H., Jansen, R. A., et al. 2023, *AJ*, **165**, 13
- Wu, C. K. W., Ling, C.-T., Goto, T., et al. 2023, *MNRAS*, **523**, 5187
- Yang, G., Papovich, C., Bagley, M. B., et al. 2023, *ApJL*, **956**, L12
- Yasuda, N., Fukugita, M., Narayanan, V. K., et al. 2001, *AJ*, **122**, 1104
- Yung, L. Y. A., Somerville, R. S., Ferguson, H. C., et al. 2022, *MNRAS*, **515**, 5416
- Zavala, J. A., Aretxaga, I., Geach, J. E., et al. 2017, *MNRAS*, **464**, 3369
- Zwicky, F. 1937, *ApJ*, **86**, 217